 CMES, vol.61, no.3, pp.201-222, 2010

# A 3D Numerical Model for a Flexible Fiber Motion in Compressible Swirling Airflow

**Hui-Fen Guo**[1,2] **and Bin-Gang Xu**[1,3]

**Abstract:** A numerical method is developed for modeling the dynamics of a flexible fiber immersed in a compressible swirling flow. The modeling approach is based on combining an Eulerian finite volume formulation for the fluid flow and a Lagrangian small-deformation formulation for the dynamics of the fiber. The fiber is modeled as a chain of beads connected through mass-less rods. The bending and twisting deformation of the fiber are represented by the displacements of the successive beads. A computational strategy is proposed for the computation of the fluid parameters at the center of discrete fiber sections. To deal with the fiber–wall interaction, a wall model is also developed. The new algorithm was verified against the experimental observations using high-speed photography. The proposed model has also been applied in a textile process to simulate the fiber motions in the two nozzles (i.e., cylindrical and diverged conical tubes, respectively) of an air-jet spinning machine, and consequently, the principle of the air-jet yarn formation can be demonstrated.

**Keywords:** compressible swirling flow, dynamic analysis, fiber motion, nozzle

## 1 Introduction

The gas-solid two-phase swirling flows have been, and still are, the subjects of intensive investigation for understanding many phenomena arising in engineering and science. Swirling flows are used in a wide range of devices such as turbines [Zhou, Chen, Xu, Ma and Guo (1998); Joseph, Vaidyanathan and Tomasz (2007)], combustion equipment [Zhou, Chen, Xu, Ma and Guo (1998); Joseph, Vaidyanathan and Tomasz (2007)], and cyclone separators using centrifugal effects in order to remove particles gas-solid mixtures (Meier and Mori 1998; Su and Mao 2006) In the 1960s, swirling airflows were also applied the textile industry, such as the rotor

[1] Institute of Textiles and Clothing, the Hong Kong Polytechnic University, Kowloon, Hong Kong
[2] College of Textile, Donghua University, Shanghai 201620, China
[3] Corresponding author, E-mail: tcxubg@inet.polyu.edu.hk

and air-jet spinning systems, to produce spun yarns. Compared with general particulates studied above [Zhou, Chen, Xu, Ma and Guo (1998); Joseph, Vaidyanathan and Tomasz (2007); Meier and Mori (1998); Su and Mao (2006)], the textile fibers not only have the large ratio of length to radius, i.e., aspect ratio, but also are elastic and flexible. In these spinning systems, due to the effects of the swirling flow, the flexible fibers are displaced and rotated around other fibers that surround them, resulting in fiber twisting and wrapping around the neighboring fibers. This motion characteristic of the fibers will help to produce a high quality yarn with good tensile strength. Therefore, the dynamics of flexible fibers in swirling flows is of great interest to predict the product properties, and to optimize the design of the spinning systems.

Numerical simulation of two-phase flows is generally dealt with using two kinds of approaches. In the Eulerian–Eulerian approach, the two phases are considered as the interacting and interpenetrating continua, whereas Eulerian–Lagrangian method involves Lagrangian monitoring of solid particles or droplets in the flow. Many studies show that although the Eulerian-Eulerian model is less time consuming and more efficient, there were fundamental flaws associated with the formulation [Durst, Milojevic and Schänung (1984); Stock (1996)]. For example, in this model, the *no-slip* boundary condition is applied for the particulate phase in wall-dominated multiphase flow; however, this is not valid for very high inertia particles. The Lagrangian approach can overcome the difficulties associated with the application of the Eulerian model for the particulate phase. It allows better consideration of the physical phenomena that govern particle motion [Durst, Milojevic and Schänung (1984); Stock (1996)]. It enables better modelling of the near-wall behavior, for instance. Therefore, a three-dimensional Eulerian–Lagrangian method is adopted for simulating fiber motion in the swirling flow in this paper.

During the past decades, some useful methods had been proposed to numerically simulate the dynamics of flexible fibers. Yamamoto and Matsuoka (1992; 1994) proposed a method in which a slender fiber is approximated by a chain of spheres connected through a spring, with additional potentials to mimic resistance to bending and twisting. This model [Yamamoto and Matsuoka (1992; 1994)] is believed to be the most suitable approach to describe the dynamics of a long flexible fiber; however, it requires enormous computational resources and computation time. To overcome such restrictions, many researchers extended Yamamoto and Matsuoka's work. Wherrett (1996) modeled a fiber as a series of cylindrical elements based on the work of Yamamoto and Matsuoka (1992; 1994) for 2D flow. The stretching and bending stiffness are modified to include the aspect ratio of the elements. Ross and Klingenberg (1997) employed a chain of rigid prolate spheroid connected through ball and socket joints to improve computation efficiency. It was further developed

by Dong, Feng, Salcudean and Gartshore (2003) to account for fiber-wall interaction. In this model, the fiber can bend and twist much like a real fiber because of the rotational freedom in each joint. Soltani and Amadi (2000) described curly fiber as five elongated ellipsoidal links to study wall deposition of fibrous aerosols in a turbulent channel flow. To simulate the dynamics of a long flexible fiber in the hydro-entanglement process, Wang et al. (2006) assumed that the flexible fiber is discretized into a chain of rigid rods, where each rod is further composed of a series of beads connecting each other. The method is extended to simulate the fiber movement in a two-dimensional turbulent flow field [Xiang and Kuznetsov (2008)]. These extended fiber models [Wherrett (1996); Ross and Klingenberg (1997); Soltani and Amadi (2000); Dong, Feng, Salcudean and Gartshore (2003); Wang, Yu and Zhou (2006); Xiang and Kuznetsov 2008)] can greatly save the computational time of long fibers. However, it is believed that too long spheroid/rod length will greatly reduce the accuracy of the simulation for a relatively flexible fiber.

In addition, some new methods have been also introduced to simulate fiber dynamics. For example, the immersed boundary method has been applied to study the interactions between fluid and solid particles [Stokie and Green (1998); Stockie (2002); Zhu and Peskin (2007)]. In this method, a fiber is discretized with connected Lagrangian markers, and their relative displacements by fluid motions are used to calculate the fiber's elastic response. To simulate the flexible fiber dynamics in a non-zero Reynolds number flow, a lattice Boltzmann method was used by Qi (2006; 2007). Other different numerical simulations of fiber dynamics were reported by Tornberg and Shelley (2004) and Fan, Phan and Zheng (1998), who employ a non-local slender body theory to capture the fluid–fiber interactions and fiber–fiber interactions.

In most of the aforementioned works, the fibers are subjected to a given simple shear flow which exerts a predetermined hydrodynamic force on the fiber. Unfortunately, little work has been reported regarding fiber dynamics in the complex compressible swirling airflow. In our previous work [Guo and Xu (2009)], a 3D bead-rod model was proposed for simulating the fiber motion in swirling airflow in a straight tube. The beads are linked to each other by inextensible rods. The bending and twisting displacements are also proposed to describe the fiber deformation. Meanwhile, the computational problem of time-consuming was solved by connecting the beads with rods instead of spheres. However, only the drag force was considered in this computation process and many essential factors, such as air compressibility, particle shape and fiber-wall collision, which may influence significantly the fiber dynamics in the swirling flow, were neglected.

Our work is concerned with problems involving fiber motion in high-speed com-

pressible swirling flows, together with a corresponding wall model, since the influence of walls is critical in the shear layer where there is large velocity gradient and centrifugal force. The bead-rod model [Guo and Xu (2009)] is extended to consider more factors, such as lift and particle-wall collision forces as well as compressible effects. To simulate motion of a flexible fiber in a flow field, the one-way coupling Euler–Lagrange approach is utilized. The flow field is first obtained by solving Favre-averaged mean Navier–Stokes equations with realizable $k$-$\varepsilon$ turbulent model using the finite-volume approach [Guo, Chen and Yu (2009); Guo and Chen (2009)], and then fiber dynamics is investigated by solving the bead–rod model equations describing the response of an elastic fiber to the combined forces exerted on it by the fluid flow. This proposed method is applied to the prediction of the motions of a flexible fiber in the two nozzles (i.e., cylindrical and diverged conical tubes, respectively) of air-jet spinning. Consequently, the principle of the air-jet yarn formation is demonstrated.

## 2 Compressible swirling flow solver

To simulate motion of a flexible fiber in a compressible turbulent swirling flow, the one-way coupling, which only considers the fluid-to-fiber effect, is utilized. The fluid phase considered here is assumed to be three-dimensional, steady, viscous turbulent flow of an ideal gas in the absence of body forces and to have constant physical properties, such as the fluid viscosity and the specific heat capacity. Fluid turbulence is modeled using the realizable $k$–$\varepsilon$ model with neglect of the influence of particle motion on fluid turbulence. The gas-phase Favre-averaged conservation equations with the gas kinetic turbulence and dissipation rate can be recast in a general form:

$$\mathrm{div}\left(\rho^g \overrightarrow{V^g}\phi - \Gamma_\phi \mathrm{grad}\phi\right) = S_\phi \tag{1}$$

Continuity equation ($\phi$= 1):

$$\Gamma_\phi = S_\phi = 0 \tag{2}$$

Momentum equation ($\phi = u_i^g$):

$$\Gamma_\phi = \mu_{eff} = \mu_l + \mu_t$$

$$S_\phi = -\frac{\partial p}{\partial x_i} + \frac{\partial}{\partial x_j}\left(\mu_{eff}\frac{\partial u_j^g}{\partial x_i}\right) \tag{3}$$

Energy equation ($\phi$= $T$):

$$\Gamma_\phi = \frac{\mu_l}{Pr} + \frac{\mu_t}{\sigma_T}$$

$$S_\phi = G_k + \rho^g (u_i^g \frac{\partial p}{\partial x_i}) \tag{4}$$

Turbulence energy equation ($\phi$= $k$):

$$\Gamma_\phi = \mu_l + \frac{\mu_t}{\sigma_k}$$

$$S_\phi = G_k - \rho^g \varepsilon - Y_M \tag{5}$$

Turbulence dissipation equation ($\phi = \varepsilon$):

$$\Gamma_\phi = \mu_l + \frac{\mu_t}{\sigma_\varepsilon}$$

$$S_\phi = \rho^g \varepsilon \mathrm{C}_1 S - \frac{\rho^g \varepsilon^2 C_2}{k + (\nu\varepsilon)^{1/2}} \tag{6}$$

Here $\phi$ is a general variable, $\Gamma$ a diffusion coefficient, and $S_{phi}$ a general source term. The vector $\overrightarrow{V^g} = (u_x^g, u_y^g, u_z^g)$ represents the fluid velocity, $\rho^g$ is the fluid density and S is the mean rate of strain tensor. $\mu_l$ and $\mu_t$ are the laminar and turbulent viscosities, respectively. $G_k$ represents the generation of turbulence kinetic energy due to the mean velocity gradients. $Y_M$ represents the contribution of the fluctuating dilatation in compressible turbulence to the overall dissipation rate. $\sigma_k$, $\sigma_\varepsilon$ and $\sigma_T$ are the turbulent Prandtl numbers for $k$, $\varepsilon$ and temperature $T$ respectively. The empirical constants are $C_2$=1.9, $C_1 = \max[0.43, \eta/(\eta+5)]$ and $\eta = Sk/\varepsilon$.

In addition, the equation of state of a perfect gas ($p$ =$\rho^g RT$) is added to complete the system of the equations.

A finite-volume method is used to discretize the continuum gas-phase governing equations on a collocated variable arrangement. Discretization of Eq. (1) on an arbitrary control volume or cell $V$ may be written as

$$\sum_f^{N_f} \rho_f^g \overrightarrow{V_f^g}_f \phi \overrightarrow{A_f} - \sum_f^{N_f} \Gamma_\phi (\nabla\phi)_{\mathrm{n}} \overrightarrow{A_f} = S_\phi V \tag{7}$$

where $N_f$ is number of faces enclosing cell, $\rho_f^g$, $\phi_f$, are the values of $\rho^g$ and $\phi$ through face $f$, respectively. $\overrightarrow{A_f}$ is area of face $f$, $(\nabla\phi)_{\mathrm{n}}$ is magnitude of $\nabla\phi$ normal to face $f$.

Due to compressible effects, the coupled implicit approach is adopted. To reduce the numerical diffusion in low-order schemes, high-order accurate schemes are employed here. For the conservation equations, the second-order upwind (SOU) schemes are applied, the face value $\phi_f$ is computed:

$$\phi_f = \phi + \nabla\phi \Delta \overrightarrow{s} \tag{8}$$

where $\phi$ and $\nabla\phi$ are the cell-centered value and its gradient in the upstream cell, and $\Delta\overrightarrow{s}$ is the displacement vector from the upstream cell centroid to the face centroid.

The generalized quadratic upstream interpolation of convective kinematics (QUICK) scheme [Leonard and Mokhtari (1990)] is used in the $k$ and $\varepsilon$ equations. For a regularly spaced grid, this scheme is of third-order accuracy, and for an irregularly spaced grid, the scheme is of second-order accuracy. For the cell '$e$' with centre $E$, the QUICK expression yields (see also Fig.1):

$$\phi_e = \theta\left[\frac{s_e}{s_p+s_e}\phi_P + \frac{s_p}{s_p+s_e}\phi_E\right] + (1-\theta)\left[\frac{s_w+2s_p}{s_p+s_w}\phi_P - \frac{s_p}{s_p+s_w}\phi_W\right] \tag{9}$$

Here points $W$ and $P$ are two points upstream of the point $E$. $S_w$, $S_p$ and $S_e$ are the lengths of the corresponding control volume of points $W$, $P$ and $E$, respectively.

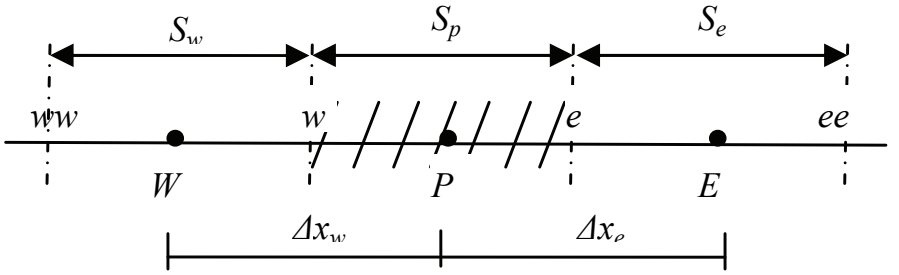


Figure 1: Computational molecule for the QUICK scheme

## 3 Flexible fiber dynamics model

A bead-rod fiber model which was developed by Guo and Xu (2009) is used in this study. The fiber is composed of $n$ beads of radius $r$ which are connected by $n$-1 mass-less rods (Fig. 2). Only the beads are affected by forces, and the rods serve to transmit forces and maintain the configuration of the fiber. Fiber extensibility is neglected in this model since it is typically small when compared with other forms of deformation. The bending and twisting deformations of the fiber are preferably described by changing the relative displacements between successive beads.

The calculation of the fiber dynamics by the Lagrangian approach requires the solution of the equation of the motion for each bead/particle. For any bead $i$, this equation includes the restoring forces (i.e., the bending restoring force $F_i^b$ and the twisting restoring force $F_i^t$), and hydrodynamic forces acting from the fluid on the bead such as drag force $F_i^d$ and shear-induced lift force $F_i^L$. Other hydrodynamic

forces such as Basset history term, added mass, slip-rotational lift force and fluid inertia are negligible here. Hence, the equations of motion for the bead $i$ are given by

$$\mathrm{d}\overrightarrow{x_i}/\mathrm{dt} = \overrightarrow{V_i^f} \quad \mathrm{m_i^f} d\overrightarrow{V_i^f}/dt = \mathrm{F_i^b} + \mathrm{F_i^t} + \mathrm{F_i^d} + \mathrm{F_i^L} \tag{10}$$

where $\mathrm{m_i^f} = \pi \mathrm{r}^2 \rho^{\mathrm{f}} (\mathrm{i_{i-1,\,i}} + \mathrm{i_{i,\,i+1}})/2$ is the mass of the bead $i$. $\rho^f$, $\overrightarrow{x_i}$ and $\overrightarrow{\mathrm{V_i^f}}$ represent density, position and velocity of the bead $i$ mass center, respectively. $l_{i-1,i}$ and $l_{i,i+1}$ are the lengths of the fiber section ($i$-1, $i$), and ($i$, $i$+1), respectively. For the mass of the end bead 1 or $n$, the mirror reflection is applied.

Different from the previous work [Guo and Xu (2009)], this study will consider more important influential factors on fiber dynamics. The local fluid density and its relevant physical variables, such as particle Reynolds number and kinematic viscosity are simulated because of the compressible effects. In addition, a wall model is employed in this analysis since the fibers frequently touch the wall in shear layer of the swirling flow.

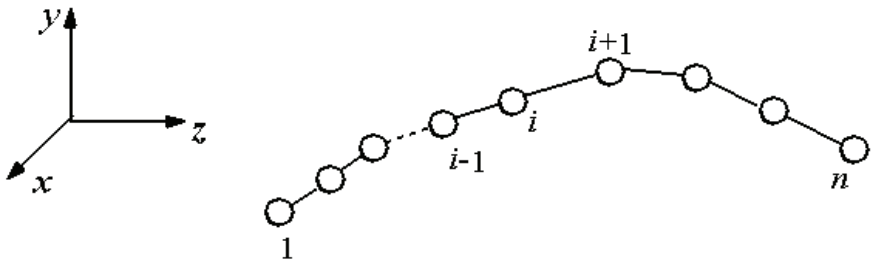


Figure 2: Schematic diagram of a fiber model

### *3.1 Restoring forces*

In this study, the fiber bend can be described by changing the displacements of three adjacent beads $i$-2, $i$-1 and $i$ (Fig. 3(a)). Assuming ($i$-1, $i_t$) is the equilibrium position of the fiber section ($i$-1, $i$) and the deformation is small, the fiber section will be bent when the bead $i$ moves from $i_t$ to $i_{t+\Delta t}$. Therefore, the bending deformation of the fiber section ($i$-1, $i$) is equivalent to that of cantilever beams. From small deflection theory [Gere and Timoshenko (1987)] the bending restoring force $F_i^b$ acting on the bead $i$ is:

$$F_i^b = -\frac{3EI_b}{l_{i-1,i}^3} s_b \tag{11}$$

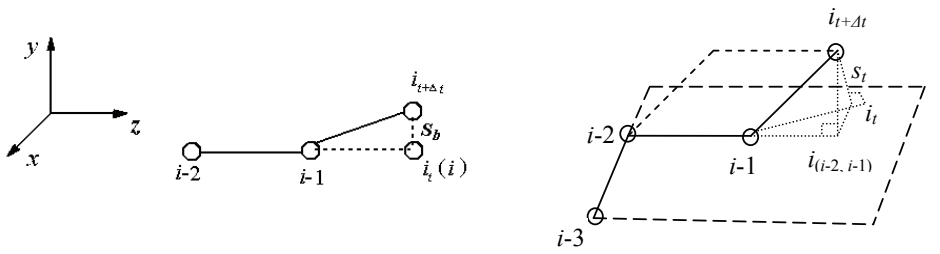


Figure 3: Sketch of the fiber deformations for (a) bending and (b) twisting

Here $s_b$ is the bending deflection of the section ($i$-1,$i$). $E$ and $I_b$ are Young's modulus and the moment of inertia of the fiber cross-section area, respectively.

Similarly, the fiber torsion can be described by changing the displacements of four adjacent beads $i$-3, $i$-2, $i$-1 and $i$ (Fig. 3(b)). Assuming fiber section ($i$-1, $i_{t+\Delta t}$) is the position after torsion of ($i$-1, $i$). The line ($i_{t+\Delta t}$, $i_t$) is normal to the plane comprising of the fiber sections ($i$-2, $i$-1) and ($i$-3, $i$-2). Point $i_{(i-2,i-1)}$ is the projection of the point $i_{t+\Delta t}$ on the line ($i$-2, $i$-1) and $l_s$ is the length of the line segment ($i_{t+\Delta t}$, $i_{(i-2,i-1)}$). According to the torsion theory of circular bar [Gere and Timoshenko (1987)], $s_t$ is the twisting displacement of the section ($i$-2, $i$-1), and the twisting restoring force $F_t^i$ acting on the bead $i$ is:

$$F_i^t = -\frac{GI_t}{l_s l_{i-2,\,i-1}} s_t \tag{12}$$

where $G$ and $i_t$ are the shear modulus and the polar moment of inertia, respectively.

### *3.2 Viscous forces in a fluid medium*

In the proposed model, the drag force $F_i^d$ and shear-induced lift force $F_i^L$ for the bead $i$ are contributed by fiber sections ($i$-1, $i$) and ($i$, $i$+1). These forces can be calculated by:

$$F_i^d = (F_{i-1,i}^d + F_{i,i+1}^d)/2 \quad F_i^L = (F_{i-1,i}^L + F_{i,i+1}^L)/2 \tag{13}$$

$F_{i-1,i}^d$ and $F_{i,i+1}^d$ are the drag forces acting on the bead $i$ and they are contributed by the fiber sections ($i$-1, $i$) and ($i$, $i$+1),respectively. $F_{i-1,i}^L$ and $F_{i,i+1}^L$ are corresponding lift forces. The drag $F_{i-1,i}^d$ acting on the fiber section ($i$-1, $i$) can be expressed as:

$$F_{i-1,i}^d = \pi d_v^2 C_D \rho^g |\overrightarrow{V_i^g} - \overrightarrow{V_i^f}| (\overrightarrow{V_i^g} - \overrightarrow{V_i^f})/8 \tag{14}$$

where $d_v = (6r^2 l_{i-1,i})^{1/3}$ is the equivalent diameter of an equal volume sphere. $\overrightarrow{\mathrm{V_i^g}}$ and $\overrightarrow{\mathrm{V_i^f}}$ are the fluid and fiber velocities at the mass center of the fiber section ($i$-1, $i$), respectively. The drag coefficient $C_D$ depends on variety parameters such as the particle size and shape, local Reynolds number, and local fluid density. Considering the effects of these factors, $C_D$ is described as [Haider and Levenspiel (1989)]:

$$C_D = \frac{24}{\mathrm{Re_p}}\left[1+\exp\left(2.3288-6.4581\Psi+2.4486\Psi^2\right)\mathrm{Re_p}^{(0.0964+0.5565\Psi)}\right]$$

$$+\frac{\exp\left(4.905-13.8944\Psi+18.4222\Psi^2-10.2599\Psi^3\right)\mathrm{Re_p}}{\exp\left(1.4681+12.2584\Psi-20.7322\Psi^2+15.8855\Psi^3\right)+\mathrm{Re_p}} \tag{15}$$

Here particle sphericity $\Psi$ ($\leq 1$) is ratio of the surface area of sphere having the same volume as the particle to the area of the particle. $\mathrm{Re_p} = \rho^g \mathrm{d_v}\left|\overrightarrow{V^g}-\overrightarrow{V^f}\right|/\mu$ is particle Reynolds number, and $\mu$ is the dynamic viscosity of the fluid. It should point out that the effects of both particle shape and local fluid density were not considered in our previous work [Guo and Xu (2009)].

Another dynamic force resulting in a deviation of particles from their trajectories is the slip–shear lift force which is induced when a particle moves with a relative velocity in a shear layer of continuous phase. In the present study, Mei (1992)'s shear-slip lift model, which stems from Saffman's work [Saffman (1965)], is adopted for higher $Re_p$, *i.e.*

$$F^L_{i-1,i} = 1.615 d_v^2 C_L (\rho^g \mu)^{\frac{1}{2}}[(\overrightarrow{V_i^g}-\overrightarrow{V_i^f})\times\overrightarrow{\omega_i^g}]/|\overrightarrow{\omega_i^g}|^{\frac{1}{2}} \tag{16}$$

with the rotation $\overrightarrow{\omega_\mathrm{i}^\mathrm{g}} = \nabla\times\overrightarrow{\mathrm{V_i^g}}$ of the fluid phase. The coefficient $C_L$ can be expressed as [Mei (1992)]:

$$\mathrm{C_{LS}} = \begin{cases}\left(1-0.3314\sqrt{\beta}\right)\exp\left(-\frac{\mathrm{Re_p}}{10}\right)+0.3314\sqrt{\beta} & \mathrm{Re_p}\leq 40\\ 0.0524\sqrt{\beta\mathrm{Re_p}} & \mathrm{Re_p}>40\end{cases} \tag{17}$$

and $\beta$ is a parameter given by

$$\beta = 0.5\mathrm{d_v}\,\overrightarrow{\omega^g}/|\overrightarrow{\mathrm{V}^{\mathrm{g}}}-\overrightarrow{\mathrm{V}^{\mathrm{f}}}|.$$

### *3.3 Wall model*

Fibers in shear layer frequently touch the wall due to both larger velocity gradient and centrifugal force of swirling flow, so a wall model that could efficiently

deal with the fiber–wall interaction is necessary. Olson (1996) and Lawryshyn (1997) developed a similar approach to deal with two-dimensional fiber-wall collision, where a reaction force is assumed to exert on the fiber to stop it passing through the solid wall and the friction force is proportional to the normal force on the fiber. In order to deal with the fiber interaction with any wall geometry, Dong, Feng, Salcudean and Gartshore (2003) developed a three-dimensional universal wall model. However, so far no well recognized wall model is available and thus a simple particle-wall collision model is adopted here. When a particle collides with the wall, the particle velocities before and after impact can be determined according to the impulse theorem as:

$$V_n^2 = -e_n V_n^1 \quad V_t^2 = e_t V_t^1 \tag{18}$$

where the superscripts 2 and 1 represent the rebound and incident components, and subscripts $n$ and $t$ are the normal and tangential directions, respectively. The variable $e$ is the particle restitution coefficient, which is a function of wall material, particle size, and incident angle [Schadeet al (2002)]. In this paper, the dependence of the normal and tangential coefficients of restitution on the collision angle, $\alpha$, was assumed to follow the relation obtained by Grant and Tabakoff (1975)

$$e_n = 0.993 - 1.76\alpha + 1.56\alpha^2 - 0.49\alpha^3$$

$$e_t = 0.988 - 1.66\alpha + 2.11\alpha^2 - 0.67\alpha^3 \tag{19}$$

It is noted that when some of a series of beads in a fiber chain collide with the wall, each collided particle is moved back to its old position at $\Delta t$ ago, and then to the location where it just touches its colliding partner. The new velocities and the new locations in the computational domain can be obtained by the wall model (Eq. (18)) and the fiber dynamics Eq. (10), respectively. However, this may break the connectivity of fiber chain. To remove this problem, the positions of beads will be slightly adjusted after impingement, as proposed by Doi and Chen (1989). A detailed calculation process was described in Section 4.

## 4 Algorithms for the fiber motion

In this section, a brief summary of the simulation procedure for evaluating the motion of a fiber in a three-dimensional compressible swirling flow is provided. In the following analysis, it is assumed that the initial fiber velocity is equal to that of the fluid at the location of the fiber centroid.

From a practical point of view, after the Eulerian computation of the fluid flow field, the Lagrangian step is performed by tracking a series of beads, with the flow quantities, such as local fluid density, velocity and rotation being calculated at the

center of each fiber section, using the data provided by the Eulerian calculation. In this simulation, a weighted moving averaging interpolation is used to obtain the fluid parameters at the center of each fiber-section from values at the closest grid nodes of the fluid finite-volume scheme.

$$z = \frac{\sum_{i=1}^{n} w_i z_i}{\sum_{i=1}^{N} w_i} \tag{20}$$

where $z$ is the unknown fluid parameter at the fiber-section center (interpolation point), and $z_i$ ($i \in 1, n$) is the corresponding quantities of the $i$th neighbor (reference) point. $N$ is the total number of neighbor points used for the averaging operation. For the $i$th point, the weight $w_i$ is a function of distance $d_i$ of the reference point to the interpolation point:

$$w_i = 1/d_i^2 \tag{21}$$

An active search sphere, which is extended from search circle [Li, Zhu and Gold (2005)], is suggested to determine the neighbor points (Fig. 4). The sphere center is located at fiber-section center and the initial radius $R_s$ can be defined as:

$$\pi R_s^2 = S_n \times (A/N_n) \tag{22}$$

where $N_n$ is the total number of the grid points and $A$ is the total area. $S_n$ is average reference point number in the sphere of radium $R_s$.

Regarding the calculation precision and cost, the total neighbor point number is $6 \leq N \leq 10$, and the reference points are sorted according to the distance from the interpolation point to the reference point. If there is more than ten points inside this search sphere, the nearest ten points will be kept as reference points. If the number

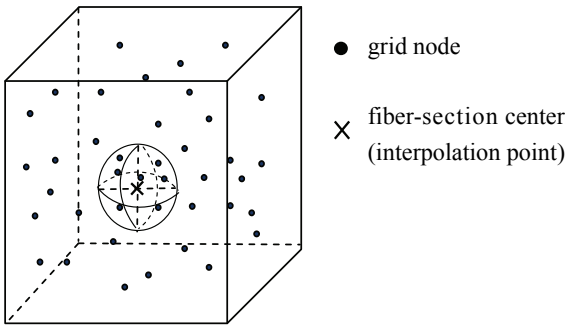


Figure 4: Active search sphere interpolation

of reference point is less than six, on the other hand, increasing radius is a necessity to achieve enough neighbor point. When such a case happens, for a set of search sphere radii $R_0 < R_1 < \ldots < R_n$, computations in the search with radius $R_i$ are discarded, but they are recalculated in the search with radius $R_{i+1}$. To reduce this loss and decrease search complexity, our algorithm retains the valuable information in the search with $R_i$ and only search the points in the range from $R_i$ to $R_{i+1}$. This is similar to a sphere decoding algorithms [Zhao and Giannakis (2004)].

When solving the dynamic Eq. (10) of the fiber, due to numerical errors and the effect of wall model, the following connectivity of the fiber chain, i.e., the nonslip conditions, may be broken.

$$\int (\overrightarrow{\mathrm{x_i}} - \overrightarrow{\mathrm{x_{i-1}}}) = \mathrm{l_f} \tag{23}$$

where $\overrightarrow{\mathrm{x_{i-1}}}$ and $\overrightarrow{\mathrm{x_i}}$ are the position vectors of adjacent beads $i$-1 and $i$, respectively. $l_f$ is the total length of the fiber.

To satisfy the nonslip conditions (23), following [Doi and Chen (1989)], the positions of the beads are slightly adjusted at each time step, i.e., the quantity of the following function becomes minimum:

$$\delta = \sum (\Delta \overrightarrow{x_i})^2 \tag{24}$$

Here, $\Delta\overrightarrow{\mathrm{x_i}}$ is the slight adjusting distance of the bead $i$.

In the paper, the time step $\Delta t$ is chosen so that the beads traverse no more than 20% of the fiber diameter in each step, which eliminates the probability of simultaneous multiple collisions. Based on the fluid field simulation, the algorithm of the fiber motion is summarized as follow:

1. Calculate the forces acting on each bead
   (a) Evaluate the fluid velocity $\overrightarrow{V^g}$, rotation $\overrightarrow{\omega^g}$ and density $\rho^g$ at each fiber section centroid using weighted averaging (Eq. (20));
   (b) Compute the drag and lift forces on each bead by Equations (13)-(17);
   (c) Calculate the bending and twisting forces for each bead by using Equations (11) and (12);
2. Calculate new coordinates and velocities of each bead at a time $t$+$\Delta t$ using Eq. (10)
3. Obtain the fiber final position at a time $t$+$\Delta t$ with the particle-wall model and geometrical constraint

(a) If bead collides with the wall, the post-collisional particle velocity and new position are calculated according to Equations (18) and (10);

(b) If no collision has occurred at all, or after all the collisions have been dealt with, the position of the bead is adjusted to satisfy the condition of Eq. (23).

## 5 Application

Air-jet spinning, as one of the application of the two-phase gas-solid swirling flow, is becoming an important spinning technique because it offers advantages in respect of processing speed, efficiency, and ability to spin fine count yarns. In this spinning system [Basu (1999); Grosberg, Oxenham and Miao (1987)], the forming yarn is 'twisted' by operating two swirling air currents in mutually opposite directions in two successive nozzles (Fig. 5(a)). The first nozzle is situated between the second nozzle and the front roller. The air in this nozzle rotates in the opposite direction to that in second nozzle. For the ribbon-like fiber bundle from the front roller, some fibers, particularly lying at the edges of the strand, are separated from the main fiber bundles, and will not be subject to the full twisting action imparted to the main body of the fibers by the swirling flow in the first nozzle and hence receive less twist than those of the main bundle. These edge fibers consequently wrap the false twisted core in the opposite direction, and form a larger twist difference between these fibers and yarn core. The fiber strand coming out of the first nozzle is then twisted by the opposite swirling flow in the second nozzle. The same amount of twist is removed from the wrapping fiber and the strand. As the yarn core is untwisted to zero twist, an opposite twist is left in the wrapping fiber, which is equal to the twist difference initially created (Fig. 5(b)). Hence, the air-jet spun yarn consists of a core of parallel fibers wrapped by surface fibers (Fig. 5(c)). However, the above-mentioned principle of yarn formation, which is mainly based on theoretical analysis and spinning experiments, still need further study. In this section, as the application of the proposed approach, the fiber motions in the air-jet spinning two nozzles are studied so that the principle of yarn formation can be demonstrated.

Due to the different functions, the first and second nozzles are made cylindrical and diverged conical shapes with the different injector number in air-jet spinning system, respectively. The swirling flows in the nozzles are created by injecting tangentially high-velocity compressed air through evenly spaced injectors placed on the periphery of the tube. Normally, the inlet pressure in the injector of the second nozzle (on the range of 3.0 to $5.0\times10^5$Pa) is higher than that of the first nozzle (2.5-$4.0\times10^5$Pa). In this study, the first and second nozzle pressures of 2.5 and $3.5\times10^5$Pa are used as the initial conditions. The Mach number approaches 1.0 near the injector outlets of the two nozzles. More information about the parameters

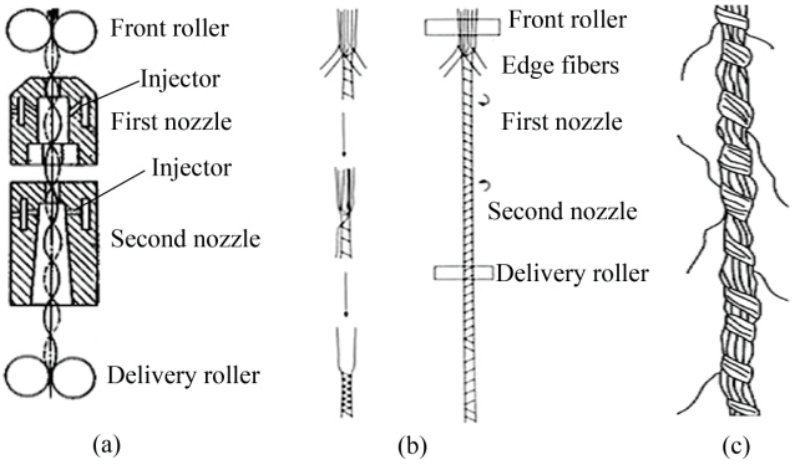


Figure 5: Schematic plots of air-jet spinning: (a) the nozzles; (b) the principle of yarn form; (c) yarn structure

and the fluid characteristics of the two nozzles has been reported in References [Guo, Chen and Yu (2009); Guo and Chen (2009)]. Only the velocity vector and streamline plots at different sections of the two nozzles are provided (Fig. 6).

As shown in Fig. 6, the airflows in the first and second nozzles are in mutually opposite directions. In the two nozzles, a reverse flow appears near the upstream wall of the injectors due to the reverse jet. The internal recirculation zones are generated as a result of the vortex breakdown in the core regions of the downstream of the two nozzles. For the first nozzle, the vortex breakdown is axisymmetric spiral type and the sense of the spiral's winding is opposite to the sense of basic flow rotation, while in the second nozzle the conical breakdown could form and its internal structure is dominated by asymmetric spiral-like vortices rotating in opposite directions. It is also to be noted, in the second nozzle, because the injectors are close to the nozzle inlet, that the velocity in upstream of injector is larger than that of slightly further the downstream of the injector. In the downstream of injector, the velocity decays quickly along axial direction for the second nozzle due to the divergence of the pipe, while the change of the velocity is not obvious in the first nozzle.

The predictions of the two simulation methods including the previous work [Guo and Xu (2009)] and present model on the fiber trajectory in the first nozzle of air-jet spinning are presented in Fig.7, where the snapshots of the fiber projections onto the *xz* plane are compared with experimental results using high-speed photography.

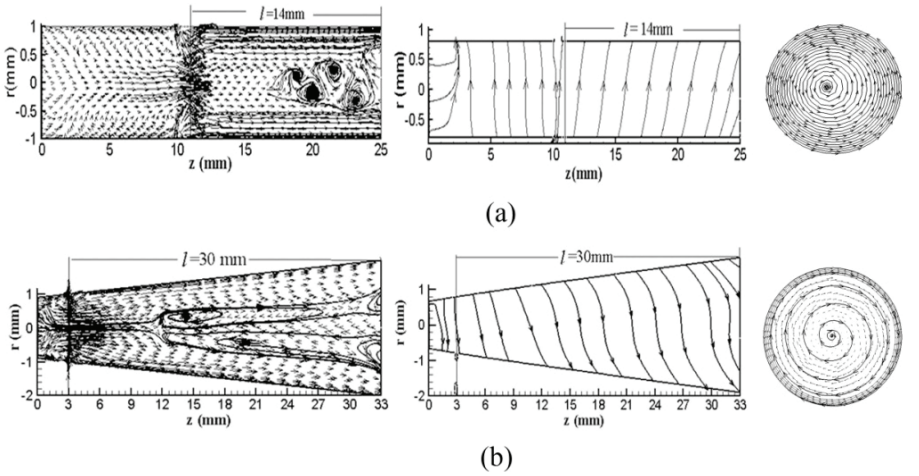


Figure 6: Predicted velocity vector and streamline plots, in order from left to right, the $y$–$z$ plane at $x$ =0mm; the $y$–$z$ plane at $x$ =0.6mm and the $x$–$y$ plane at $z$=21mm and $z$=4mm for (a) the first nozzle and (b) the second nozzle. $l$ is the distance from the injector to the outlet.

It is clear that the present simulation results (Fig. 7(b)) are in good agreement with the experimental observations (Fig. 7(c)), while the previous results (Fig. 7(a)) only have qualitative agreements. In addition, comparison of the Figs. 7(a) and 7(b) show that the deformation of the fiber in the present model is fairly flexible. In these senses, these factors including the change of the density, lift force and wall model play an important role in studying the fiber dynamics in compressible swirling flow. It is seen from Fig.7(b) that the evolution of the fiber configuration is complex during the whole period. In upstream of the injectors, the leading end of the fiber move toward the wall and it bends like a snake shape. After its leading end enters into the recirculation zone near the upstream wall of the injectors, the fluid can exert a greater compressive stress on the fiber due to low velocity reverse flow (see also Fig. 6(a)), inducing a larger buckling. This curved fiber then is stretched when it passes through the high velocity zone of downstream of the injectors and enters into the breakdown zone. Finally, the fiber forms a helix and rotates like a corkscrew in the breakdown zone.

To demonstrate the principle of air-jet yarn formation, the fiber motions releasing at three different locations in two air-jet spinning nozzles are simulated. The initial position of the fiber is parallel to the stream-wise direction and its length is assumed to be 4mm. The tailing end beads of the fibers are initially released at the nozzle

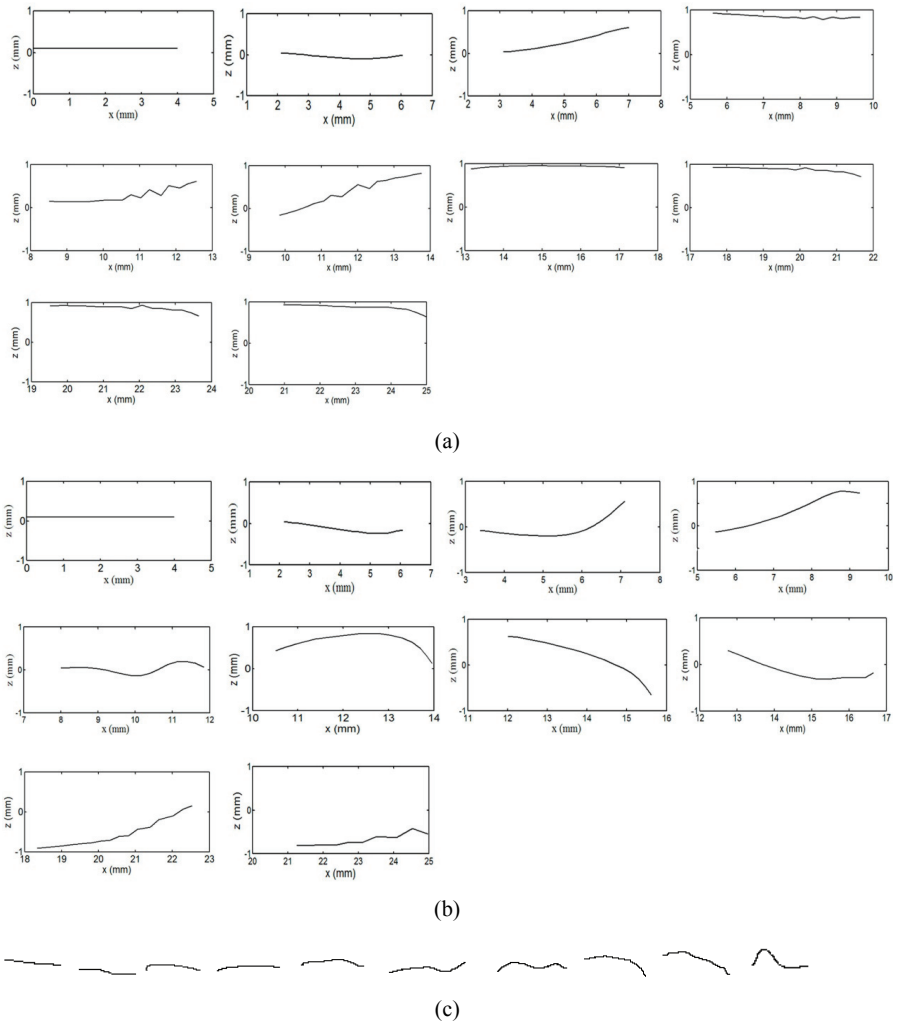


Figure 7: Snapshots of fiber motion in the swirling flow of the first nozzle (a) projections onto the *xz* plane for simulation without variable density, lift force and wall model [Guo and Xu (2009)]; (b) projections onto the *xz* plane for simulation with variable density, lift force and wall model (present model); (c) experimental measurements using high-speed photography.

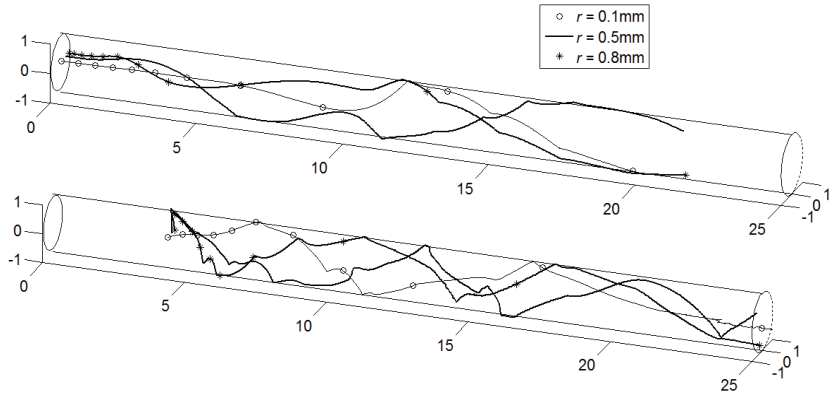


(a)

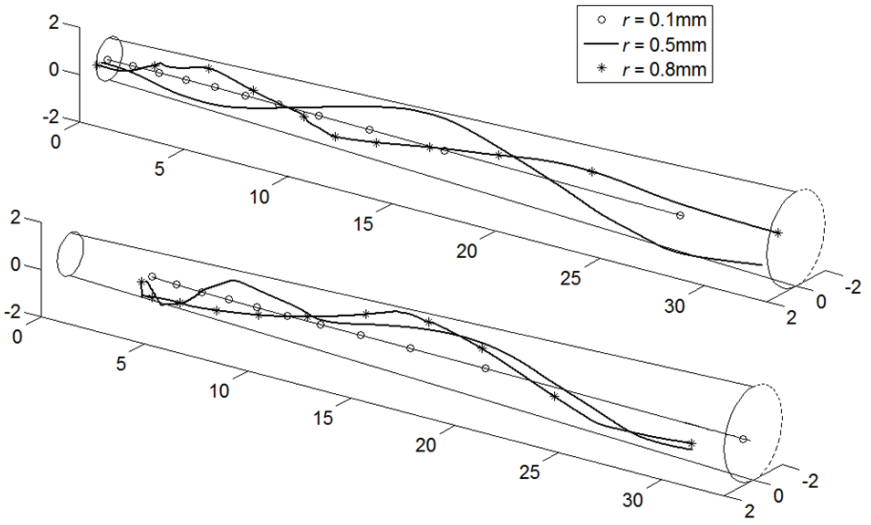


(b)

Figure 8: The trajectories of the leading end and tailing end beads in a fiber chain starting at the nozzle inlets and three different radii $r$ = 0.1, 0.5 and 0.8mm for (a) first nozzle; (b)second nozzle. Empty-circle lines (o-), solid lines (-) and asterisk lines (*-) represent the releasing positions of the fiber at $r$ = 0.1, 0.5 and 0.8mm, respectively. Upper figure, the tailing end bead; and lower figure, the leading end bead.

inlet and at three different radii $r = 0.1$, 0.5 and 0.8mm (which the nozzle inlet radii in the first and second nozzles are 1mm and 0.9mm, respectively).

Figure 8 depicts the trajectories of the leading end and tailing end beads of a fiber chain starting at three different radii $r = 0.1$, 0.5 and 0.8mm in the first and second nozzles. They are all helical except the trajectory of the fiber in the core zone of the second nozzle, and the screw-pitch increases rapidly with the stream-wise direction, especially, in downstream of the injectors. It can be observed from Figure 8 that due to the centrifugal effects of the swirling flow, the closer the releasing position of the fiber is to the wall, the earlier the trajectory of the fiber starts to swirl. As a result, a larger twist difference between the fibers of the different level, especially between the edge fiber and the core one, is formed.

As seen from Fig. 8(a), in the first nozzle, the trajectory of the fiber closest to the center ($r = 0.1$, i.e., empty-circle lines in Fig. 8(a)) starts to bend near the injectors, and it rotates in the opposite direction to that of outer fibers ($r = 0.5$ and 0.8, i.e., solid and asterisk lines in Fig. 8(a)). This demonstrates the function of the first nozzle, in which the initial wrap of the edge fibers is twisted in a direction opposite to that of the core fibers [Grosberg, Oxenham and Miao (1987)]. Similarly, for the second nozzle (Fig. 8(b)), the center particle trajectory is nearly straight or little crimple, and forms an untwisted (parallel) fiber core. Comparison of upper and lower figures in Fig. 8(b), for the fibers near the wall ($r = 0.5$ and 0.8), their tailing end is near the nozzle outlet, while the leading end is in the inner zone of the nozzle, as any bead of the fiber chain arrives at the nozzle outlet. This indicates that these fibers have one or two ends will embed in the yarn core to support a tensile load. Hence, when the yarn is subjected to a tensile load, these fibers are subjected to a stress proportional to the yarn tensile load, and they contribute to yarn strength [Rajamanickam, Patel, Hansen and Jayaraman (1998)]. According to our simulation results, i.e., the fiber motions in the two nozzles (compressible swirling flow), the principle of yarn formation can be demonstrated and a yarn structure which an untwisted core of parallel fibers are wrapped by surface fibers is formed.

## 6 Conclusions

We have proposed a method for modeling the dynamic behavior of the fiber in compressible swirling airflow. The fiber model describes the character of large aspect ratio, elasticity and flexibility of the fiber which are defined by the bending and twisting displacements (in Section 3.1). Mathematical model is developed using one-way Euler–Lagrange approach, which treats the swirling airflow by the Euler finite volume approach and predicts the fiber motion by the Lagrange approach. A weighted moving averaging method based on active search sphere is used to obtain

the fluid parameters at the center of discrete fiber sections. The experimental formulas obtained by Grant and Tabakoff (1975) are adopted to deal with particle-wall collision.

The proposed approach is applied to simulate a fiber motion in the two nozzles of an air-jet spinning machine in textile processing. The simulation results for fiber motion in the first nozzle are consistent with the experimental observation. Again, the principle of air-jet yarn formation is also demonstrated by the motions of the fibers releasing on different positions in the two nozzles. From these results, it was confirmed that the proposed method was convenient to simulate the dynamic behavior of flexible fiber in a compressible flow field. However, the model is one-way coupling, which only considers the effects of the flow field on the fiber. To obtain a more clear understanding on the interaction between the fiber and airflow, the two-way coupling algorithm must be developed. Further study will focus on this subject.

**Acknowledgement:** The authors wish to acknowledge the funding support from the Hong Kong Polytechnic University for the work reported here.

## References

**Basu, A.** (1999): Progress in air-jet spinning. *Textile Progress*, vol.29, no. 3, pp. 1-38.

**Doi, M.; Chen, D.** (1989): Simulation of aggregating colloids in shear flow. *J. Phys. Chem.*, vol.90, pp. 5271-5279.

**Dong, S.; Feng, X.; Salcudean, M.; Gartshore, I.** (2003): Concentration of pulp fibers in 3d turbulent channel flow. *J. Multiphase Flow*, vol.29, pp. 1–21.

**Durst, F.; Milojevic, D.; Schänung, R.** (1984): Eulerian and Lagrangian predictions of particulate two-phase flows: a numerical study. *Appl. Math. Model.*, vol.8, pp. 101–115.

**Fan, X.; Phan-Thien, N.; Zheng, R.** (1998): A direct simulation of fiber suspensions. *J. Non-Newtonian Fluid Mech.*, vol. 74, no. 1-3, pp. 113-135.

**Gere, J.M.; Timoshenko, S.P.** (1987): Mechanics of Materials. *2nd ed. Van Nostrand, Reinhold, London*.

**Grant, G.; Tabakoff, W.** (1975): Erosion prediction in turbomachinery resulting from environmental solid particles. *J. Aircraft* , vol.12, no. 5, pp. 471-478.

**Grosberg, P.; Oxenham, W.; Miao, M.** (1987): The insertion of 'twist' into yarns by means of air-jets. part I: an experimental study of air-jet spinning. *J. Text. Inst.*, vol. 78, no. 3, pp. 189-203.

**Guo, H.F.; Xu, B.G.** (2009): A novel method for dynamic simulation of flexible fibers in a 3D swirling flow. *Int. J. Nonlinear Sci. Num. Simul.*, vol. 10, no. 11-12, pp. 1473-1479.

**Guo, H.F.; Chen, Z.Y.; Yu, C.W.** (2009): 3D Numerical simulation of compressible swirling flow induced by means of tangential inlets. *Int. J. Numer. Methods Fluids*, vol. 59, no. 11, pp. 1285-1298.

**Guo, H.F.; Chen, Z.Y.** (2009): Numerical simulation of tangentially injected turbulent swirling flow in a divergent tube. *Int. J. Numer. Methods Fluids*, vol. 61, no. 7, pp. 796–809.

**Haider, A.; Levenspiel, O.** (1989): Drag coefficient and terminal velocity of spherical and non-spherical particles. *Power Technology*, vol. 58, pp. 63-70.

**Joseph, C.O.; Vaidyanathan, S.; Tomasz, G.D.** (2007): Large eddy simulation of swirling particle-laden flow in a model axisymmetric combustor. *Proc. Combustion Institute*, vol. 31, no. 2, pp. 2291-2299.

**Lawryshyn, Y.A.** (1997): Statics and dynamics of pulp fibers, Ph.D. thesis, University of Toronto.

**Leonard, B.P.; Mokhtari, S.** (1990): Ultra-sharp nonoscillatory convection schemes for high-speed steady multidimensional flow. *NASA technical memorandum 102568 (ICOMP-90-12), NASA Lewis Research Center*.

**Li, Z.; Zhu, Q.; Gold, C.** (2005): Digital terrain modeling: principles and methodology. *CRC Press*.

**Mei, R.** (1992): An approximate expression for the shear lift force on a spherical particle at finite Reynolds number. *Int. J. Multiphase Flow*, vol. 18, pp. 145–147.

**Meier, H. F.; Mori, M.** (1998): Gas-solid flow in cyclones: The Eulerian-Eulerian approach. *Comput. Chem. Engrg.*, vol.22, no. 1, pp. S641-S644.

**Olson, J.S.** (1996): The effect of fiber length on passage through narrow apertures, Ph.D. thesis, University of British Columbia.

**Qi, D.W.** (2006): Direct simulations of flexible cylindrical fiber suspensions in finite Reynolds number flows. *J. Phys. Chem.*, vol. 125, no. 11, pp. 114901-1-10.

**Qi, D.W.** (2007): A new method for direct simulations of flexible filament suspensions in non-zero Reynolds number flows. *Int. J. Numer. Methods Fluids*, vol. 54, pp. 103–118.

**Rajamanickam, R.; Patel, M.; Hansen, S.M.; Jayaraman, S.** (1998): Interaction of process and material parameters in air-jet spinning. *Textile Res. J.*, vol. 68, no. 10, pp. 708-714.

**Ross, R.; Klingenberg, D.** (1997): Dynamics simulation of flexible fibers com-

posed of linked rigid bodies. *J. Phys. Chem.*, vol.106, pp. 2949–2960.

**Saffman, P.G.** (1965): The lift on a small sphere in a shear flow. *J. Fluid Mech.*, vol. 22, no. 2, pp. 385-400.

**Schade, K.P.; Erdmann, H.J.; Hadrich, Th.; Schneider, H.; Frank, Th.; Bernert, K.** (2002): Experimental and numerical investigation of particle erosion caused by pulverised fuel in channels and pipework of coal-fired power plant. *Powder Technology* , vol. 125, pp. 242–250.

**Soltani, M.; Ahmadi, G.** (2000): Direct numerical simulation of curly fibers in turbulent channel flow. *Aerosol Sci. and Technol.*, vol.33, pp. 392–418.

**Stokie, J.M.; Green, S.I.** (1998): Simulating the motion of flexible pulp finer using the immersed boundary method. *J. Comput. Phys.*, vol. 147, pp. 147–165.

**Stockie, J.M.** (2002): Simulating the dynamics of flexible wood pulp fibres in suspension. *Proc. 16th Annual Int. Symp. High Perform. Computing Systems Appl., Moncton, NB.* pp.145-151.

**Su, Y.X.; Mao, Y.** (2006): Experimental study on the gas–solid suspension flow in a square cyclone separator. *Chem. Engrg J.*, vol. 121, no. 1, pp. 51-58.

**Stock, D.E.** (1996): Particle Dispersion in Flowing Gases-1994 Freeman Scholar Lecture. *J. Fluids Engrg.-Trans. ASME*, vol. 118, no. 1, pp. 1–17.

**Tornberg, A.K.; Shelley, M.J.** (2004): Simulating the dynamics and interactions of flexible fibers in Stokes flows. *J. Comput. Phys.*, vol. 196, no. 1, pp. 8-40.

**Wang, G.; Yu, W.; Zhou, C.** (2006): Optimization of the rod chain model to simulate the motion of a long flexible fiber in simple shear flows. *European J. Mech. B/Fluids*, vol. 25, pp. 337–347.

**Wherrett, G.** (1996): Fiber motion in shear flow, M.A. Sc. thesis, University of British Columbia.

**Xiang, P.; Kuznetsov, A.V.** (2008): Simulation of shape dynamics of a long flexible fiber in a turbulent flow in the hydro-entanglement process. *Int. Commun. Heat Mass Transfer*, vol. 35, no. 5, pp. 529-534.

**Yamamoto, S.; Matsuoka, T.** (1992): A method for dynamics simulation of rigid and flexible fibres in a flow field. *J. Phys. Chem.*, vol. 98, pp. 644–650.

**Ymamoto, S.; Matsuoka, T.** (1994): Viscosity of dilute suspensions of rodlike particles: a numerical simulation method. *J. Phys. Chem.*, vol. 100, pp. 3317–3324.

**Zhao, W.L.; Giannakis, G.B.** (2004): Sphere decoding algorithms with improved radius search. *IEEE Trans. Wireless Commun. Netw. Confer.* pp. 2290-2294.

**Zhou, L. X.; Chen, T.; Xu, Y.; Ma, Z. H.; Guo, Y. C.** (1998): Strongly swirling

gas-particle flows and coal combustion in a cyclone combustor. *Twenty-seventh Sympo. Int. Combustion*, vol. 27, no. 2, pp. 3119-3126.

**Zhu, L.D.; Peskin, C.S.** (2007): Drag of a flexible fiber in a 2D moving viscous fluid. *Computers Fluids*, vol. 36, no. 2, pp. 398-406.